Periprostatic adipose tissue displays a chronic hypoxic state that limits its expandability

Mathieu Roumiguié, David Estève, Cécile Manceau, Aurélie Toulet, Jérôme Gilleron, Chloé Belles, Yiyue Jia, Cynthia Houël, Sarah Pericart, Sophie Legonidec, et al.

Periprostatic adipose tissue displays a chronic hypoxic state that limits its expandability

Mathieu Roumiguié, David Estève, Cécile Manceau, Aurélie Toulet, Jérôme Gilleron, Chloé Belles, Yiyue Jia, Cynthia Houël, Sarah Pericart, Sophie LeGonidec, Philippe Valet, Mireille Cormont, Jean-François Tanti, Bernard Malavaud, Anne Bouloumié, Delphine Milhas, Catherine Muller

PII: S0002-9440(22)00108-0

DOI: https://doi.org/10.1016/j.ajpath.2022.03.008

Reference: AJPA 3723

To appear in: *The American Journal of Pathology*

Received Date: 20 December 2021

Revised Date: 15 February 2022

Accepted Date: 8 March 2022

Please cite this article as: Roumiguié M, Estève D, Manceau C, Toulet A, Gilleron J, Belles C, Jia Y, Houël C, Pericart S, LeGonidec S, Valet P, Cormont M, Tanti J-F, Malavaud B, Bouloumié A, Milhas D, Muller C, Periprostatic adipose tissue displays a chronic hypoxic state that limits its expandability, *The American Journal of Pathology* (2022), doi: https://doi.org/10.1016/j.ajpath.2022.03.008.

Periprostatic adipose tissue displays a chronic hypoxic state that limits its expandability

Running title: Periprostatic fat displays hypoxia

Mathieu Roumiguié[1,2#], David Estève[1#], Cécile Manceau[1,2], Aurélie Toulet[1], Jérôme Gilleron[3], Chloé Belles[4], Yiyue Jia[1], Cynthia Houël[1], Sarah Pericart[5], Sophie LeGonidec[6], Philippe Valet[6], Mireille Cormont[3], Jean-François Tanti[3], Bernard Malavaud[2], Anne Bouloumié[4], Delphine Milhas[1], Catherine Muller[1]
# Equal Contribution

[1] Institut de Pharmacologie et de Biologie Structurale (IPBS), Université de Toulouse, CNRS, Toulouse, France. Équipe Labélisée Ligue Nationale contre le Cancer.
[2] Département d'Urologie, Institut Universitaire du Cancer, 31059 Toulouse Cedex 9, France.
[3] Université Côte d'Azur, INSERM, C3M, Team "Cellular and Molecular Pathophysiology of Obesity", Nice, France.
[4] Institut des Maladies Métaboliques et Cardiovasculaires (I2MC), Université de Toulouse, INSERM, UPS, Toulouse, France.
[5] Département d'Anatomo-Pathologie, Institut Universitaire du Cancer, 31059 Toulouse Cedex 9, France.
[6] Institut RESTORE, Université de Toulouse, CNRS U-5070, EFS, ENVT, INSERM U1301, Université Paul Sabatier, Toulouse, France.

Address correspondence to : Catherine Muller, IPBS CNRS UMR 5089, 205 route de Narbonne, 31077 Toulouse, France. Phone : 33.561.17.59.32; E-mail : muller@ipbs.fr or to : Delphine Milhas, IPBS CNRS UMR 5089, 205 route de Narbonne, 31077 Toulouse. Phone: 33-561-17-58-66, E-mail: delphine.milhas@ipbs.fr

Conflict of interest: The authors have declared that no conflict of interest exists.

Fundings: This study was supported by the Ligue Nationale Contre le Cancer (Équipe labélisée), the French National Cancer Institute (INCA PL-BIO 2016-176 to PV, BM and CM), by the Fondation Toulouse Cancer Santé (to PV, BM and CM) and by the Fondation ARC (Association de Recherche contre le Cancer) Programmes labelisés 2016 (to PV, BM and CM). DE received a post-doctoral fellowship from the Fondation pour La Recherche Médicale (SPF201809007124).

Abstract

White adipose tissue accumulates at various sites throughout the body and some adipose tissue depots exist in close proximity to organs, whose function they could influence in a paracrine manner. Prostate gland is surrounded by a poorly characterized adipose depot called periprostatic adipose tissue (PPAT) playing emerging roles in prostate-related disorders. Unlike all other adipose depots, PPAT secretes pro-inflammatory cytokines even in lean individuals and does not increase in volume during obesity. These unique features remain unexplained due to the poor structural and functional characterization of this tissue. We characterized the structural organization of PPAT in patients in comparison to abdominopelvic adipose tissue (APAT), an extraperitoneal adipose depot whose accumulation is correlated to BMI. Confocal microscopy followed by 3D reconstructions showed a sparse vascular network in PPAT when compared with that in APAT, suggesting that this tissue is hypoxic. Unbiased comparisons of PPAT and APAT transcriptomes found that most differentially expressed genes were related to the hypoxia response. High levels of the hypoxia-inducible factor HIF-2α confirmed the presence of an adaptive response to hypoxia in PPAT. This chronic hypoxic state was associated with inflammation and fibrosis, which were not further upregulated by obesity. This fibrosis and inflammation explain the failure of PPAT to expand in obesity and open new mechanistic avenues to explain its role in prostate-related disorders including cancer.

Keywords: Periprostatic adipose tissue; Prostate cancer; Hypoxia Inducible Factor; Extracellular Matrix; Inflammation

Introduction

In mammals, white adipose tissue (WAT) accumulates at various sites throughout the body. The most important and well-studied fat deposits occur in subcutaneous regions (SC-AT) and in the abdominal cavity surrounding key internal organs, such as the intestines, deposit named visceral adipose tissue (VAT) [1]. WAT comprises metabolically active adipocytes and other cell types in the stroma vascular fraction including adipose progenitor cells, fibroblasts, mural, endothelial and immune cells, all of which are embedded in the extracellular matrix (ECM) [1]. Studies of these two WAT have been mainly centered on their role in controlling energy homeostasis in response to systemic nutritional and metabolic needs and metabolic differences have been highlighted between these two fat depots [2]. In addition to these major adipose tissues (AT), other adipose depots are distributed across the body such as for example, mammary adipose tissue (MAT), epicardial, perivascular and bone-marrow ATs [1]. These ATs are frequently closely associated with other anatomical structures and emerging evidences show that they play a paracrine role in proximal organ specific functions during pathological process such as regenerative or infectious disorders as well as cancers [1,3]. However, despite their growing importance, for most of them, their biology remains poorly described.

Periprostatic adipose tissue (PPAT) belongs to these specific adipose depots. PPAT surrounds the prostate gland and is separated from it by a fibromuscular sheet of varying thickness called the prostate "capsule"; nearly one third of the anterior surface of the glandular tissue, however, is in direct contact with the PPAT [4,5]**.** PPAT is often considered to be VAT although it is located in the pelvic region. Characterization of this tissue in any species remains poor but at least two characteristics of PPAT indicate that it is distinct from other WAT. First, it does not increase in volume even when other forms of WAT (including VAT) are present in excess in obesity [6] . Second, PPAT secretes large amounts of pro-inflammatory cytokines such as IL-

6 and TNFα [6–8]. Whereas this chronic inflammatory state is usually observed in WAT of obese patients [9], in PPAT it is independent of the state of obesity of the individual [10–12]. PPAT has received increasing attention these last years since we and others have demonstrated that PPAT plays a paracrine role in prostate cancer (PCa) progression implicating soluble factors (such as pro-inflammatory cytokines, chemokines) as well as lipid mediators [4,13,14]. Molecules released by PPAT could also impact normal prostate development and contractility and contribute to benign prostatic hyperplasia (BPH) and related symptoms as recently proposed [15]. A better understanding of PPAT biology is mandatory to provide a foundation for further mechanistic inquiries on its paracrine role on prostate.

Accordingly, the initial goal of this study was to characterize the structural organization of PPAT in patients; by doing so, we have obtained new functional insights. We report here that PPAT has a sparse vascular network responsible for a chronic hypoxic state leading to inflammation, as well as fibrosis that is independent of obesity. These structural and functional characteristics explain the failure of PPAT to expand in obesity and open new mechanistic avenues to explain its role in prostate disorders including cancer.

Materials and Methods

Patients and fat measurements

Between September 2016 and March 2021, patients with localized PCa diagnosed by prostate biopsies who were opting for radical prostatectomy were recruited. We excluded from the study patients with metastatic PCa (as assessed by computerized tomography and/or bone scan), and patients who had received radiotherapy, hormonal or high intensity ultrasound treatment. As controls for the experiments to investigate the 3D vasculature (see below), PPAT

samples were obtained from two patients undergoing radical cysto-prostatectomy for muscle-invasive bladder cancer and who lacked PCa according to the pathologist's report.

All the patients underwent pre-operative 1.5 T mpMRI after injection with 20 mg of butyl scopolamine (Buscopan; Boehringer-Ingelheim, Paris, France). Anatomic 3D fast spin echo T2-weighted MRI, functional diffusion-weighted MRI and dynamic contrast-enhanced MRI data were acquired. After anonymization of the mpMRI data, the Subcutaneous fat thickness (SFT) and the PPAT and APAT volumes were measured in 54 patients by using a semi-automated segmentation technique on contiguous 3 mm T2-weighted axial slices (except for SFT where one slice was used) and Olea Sphere software (Olea medical, La Ciotat, France). Baseline demographic characteristics (age and body mass index (BMI), disease specific parameters (Gleason score and histopathological stage of radical prostatectomy specimens) and mpMRI data were acquired from the medical records of the patients. The clinical characteristics of the cohort is presented in Supplemental Table S1. One observer, trained by a senior experienced radiologist and blind to the clinical and pathological data, carried out all segmentations and measurements. The PPAT was segmented from the level of the prostate base to the apex (see Figure 1A) (mean 14 slices per patient). The following anatomical boundaries were used to define PPAT limits on each slice: pubic symphysis at the front, obturator muscles on the lateral sides and Denonvilliers fascia at the back. APAT was measured by segmenting the fat located above the pubic symphysis, in front of the bladder and behind the abdominal muscles and included between each spermatic cordon on the lateral sides (mean 3 slices per patient). SFT was determined by measuring the perpendicular distance between the skin and the anterior upper border of the symphysis pubis on a selected T2-weighted axial slice.

Tissue collection and tissue processing

Paired anterior PPAT and APAT from patients undergoing radical prostatectomy were removed and the samples were anonymized. Charred samples and those weighing < 300 mg were excluded from the study. Samples were immediately put in 50 ml tubes containing 10 ml of Dulbecco's Modified Eagle's Medium (DMEM, Thermofischer scientific, Courtaboeuf, France) and were transported to the research lab within 1 h, except for the western blotting experiments where the samples were immediately placed in 100 µl of RIPA lysis buffer containing phosphatases and proteases inhibitors (all from Sigma-Aldrich, St Quentin Fallavier, France) in the operating theatre. The samples were weighed and use for several preparations. For qPCR analysis and dosage of hydroxyproline content, paired PPAT and APAT were immediately frozen in liquid nitrogen and stored at -80°C for later use. For 3D microscopy and lobule size analysis, samples were either embedded in paraffin for measuring adipocyte size as previously described [16] and for Masson's Trichrome stain, or were fixed with 4% paraformaldehyde solution at room temperature for 24 hours. Lobules were dissected as previously described [17]. Some of the samples were also used to isolate the stroma vascular fraction after collagenase digestion (see below). Finally, samples were used to prepare PPAT- or APAT-conditioned medium as previously described [13]. Briefly, 1 g of tissue was incubated overnight in 8 ml of DMEM supplemented with 1% BSA in a humidified incubator at 37°C and with 5% CO_2 and the medium was collected after filtration through a 0.2 µM filter. The conditioned media were immediately stored in small aliquots at -80°C.

RNA extraction and qRT-PCR

For RNA extraction, 100 mg of frozen tissue was mixed with 500 µl QIAzol lysis reagent (Qiagen, Hilden, Germany) and homogenized with a Precellys tissue homogenizer (2 cycles of 45 s at 7500 rpm at 4°C) using the Cryolys cooling system (Bertin Technologies, Montigny le

Bretonneux, France). RNA were extracted using the Qiagen RNeasy mini kit and cDNA were reverse transcribed from 250 ng of purified RNA by using the ReverAid H Minus First Strand cDNA synthesis kit (Thermo Fisher Scientific) with hexamer random primers according to the supplier's recommendations. Gene expression was quantified by quantitative RT-qPCR with TaqMan primers (*VEGFA*: Hs00900055_m1, *VEGFB*: Hs00173634_m1, Thermo Fisher Scientific) and Fast Advanced TaqMan Master Mix (Thermo Fisher Scientific) with a CFX96 real time PCR system (Bio-Rad, Marnes la Coquette, France). Results were normalized to the amount of 18S rRNA.

RNA sequencing and data preprocessing

RNA-Seq libraries were generated from 400 ng of total RNA by using the TruSeq Stranded mRNA LT Sample Preparation Kit (Illumina, San Diego, CA), according to the manufacturer's instructions. The cDNA libraries were sequenced on an Illumina HiSeq 4000 system using single-read 50 bp following Illumina's recommendations. Preprocessed reads were mapped onto the *Homo sapiens* genome assembly hg38 by using STAR v2.5.3a [18]. Gene expression was quantified from uniquely aligned reads by using HTSeq-Count (v0.6.1p1) with annotations from Ensembl (v91) and "union" mode2. Only unambiguously assigned reads were retained for further analyses. Datasets generated during this study have been deposited in the gene expression omnibus (GEO) database https://www.ncbi.nlm.nih.gov/geo/ and are available under accession number GSE196442.

Normalized gene expression was log2 transformed and used to perform principal component analysis with the FactomineR package (v1.42) within R (v3.6). Statistical analysis of differentially expressed genes was performed with the Limma package (v3.40.2) Gene expression was considered significantly different if the p-value was < 0.05 and the log2 fold-

change was > 2 or < -2. Pathway enrichment analysis was performed with GSEA software using the official gene symbols and 'hallmark' gene sets in the Molecular Signatures database (v7.3). Overlap between differentially expressed genes and curated gene sets or hallmark gene sets were computed. Heatmaps were made with Ward's hierarchical clustering method by using the gplots package (v3.0.1.1). Protein–protein interaction networks were created by using Cytoscape (v3.7.1) and ClueGo plugin.

Tridimensional vasculature imaging of adipose tissues

To study the tridimensional vasculature of adipose tissues, we used a clearing method suited to investigate the morphology of WAT by fluorescence imaging, which we described recently[19]. Briefly, the tissues were stained with anti-CD31–Alexa Fluor 647 antibody (Miltenyi Biotech, Paris France), DAPI (5 μg/ml) and phalloidin–Alexa Fluor 488 (Invitrogen, Courtaboeuf, France). The 3D image stacks were acquired in a mosaic by using a Nikon-A1R confocal microscope equipped with a 20X long-distance air objective and analyzed with Imaris software (Bitplane, Gometz la Ville, France).

Hydroxyproline quantification

Fragments of adipose tissue of about 100 mg were weighed precisely and then placed in 500 μl deionized water in a Precellys 2 ml Soft Tissue homogenizing Ceramic beads Kit (CK14) and extracted by using the Precellys tissue homogenizer with 2 cycles of 45 s at 7500 rpm at room temperature. Samples were then centrifuged for 10 min at 5000 g at room temperature to remove lipids floating on the top layer by pipetting. Lipid-free supernatants were vortex mixed, 150 μl were mixed with an equal volume of 10 M NaOH and heated at 105°C for 1 h to fully digest collagens. The reaction was stopped by adding 150 μl of 10M HCl. Hydroxyproline

was quantified in duplicate by using the Hydroxyproline Assay Kit (Perchlorate-Free; Biovison™, Milpitas, CA) as recommended by the supplier and normalized to the precise tissue weight initially digested.

Masson's Trichrome stain, collagen staining with Picrosirius Red and 3D collagen fiber quantification

For Masson's Trichrome staining, adipose tissues were deparaffinized with xylene for 5 min, dehydrated in 100% alcohol for 5 min, and then rehydrated in running tap water for 5–10 min. The tissues were first stained in Mayer's hemalum solution for 20 min and washed in distilled water and in ammonia water each for 30 seconds. Then they were stained in Ponceau S solution for 1 min and washed in distilled water. They were differentiated in 1% phosphomolybdic solution for 5 min, transferred to aniline blue solution and stained for a further 5 min. The tissues were rinsed briefly in distilled water and differentiated in 1% acetic acid solution for 4 min, then dehydrated rapidly through alcohol and cleared in xylene. For collagen staining with Picrosirius Red, fixed adipose tissues were incubated for 3 h in PicroSirius Red solution (1 g/l Sirius red in 1. 3 % picric acid). After two washes in acidified water followed by fixation/dehydration steps in 100 % ethanol, images were taken with a Zeiss LSM710 confocal microscope equipped with a 40x oil-immersion inverted objective with a numerical aperture of 1.3. The samples were excited at 560 nm and fluorescence emission was collected above 580 nm. Pinhole was setup at 0.7 Airy (ZEISS ZEN imaging software, Oberkochen, Germany) to increase resolution. 3D reconstructions and analyses of collagen fiber organization were performed with Imaris software and the Filament Tracer module. The data generated were normalized to the tissue volume obtained after tissue surface reconstruction with Imaris.

Western blotting

For western blotting, 100 mg samples of PPAT or APAT were immediately incubated with 100 µl of RIPA lysis buffer containing phosphatases and proteases inhibitors (from Sigma Aldrich) before transportation to the research lab. Proteins were extracted using the Precellys tissue homogenizer and Soft Tissue homogenizing Ceramic beads (CK14) with 2 cycles of 45 s at 7500 rpm at room temperature. The samples were then centrifuged 10 min at 10 000 g at room temperature to separate the lipids. The extract was recovered without the lipid layer and centrifuged again 10 min at 10 000 g at 4°C. In some experiments, proteins were extracted from the prostate cancer cell line PC3 before or after treatment with 200 µM cobalt chloride for 16 h, as previously described [14]. Proteins in the extracts (40 µg for tissues and 20 µg for PC3 cells) were separated by electrophoresis on a 4–10% gradient SDS-PAGE gel (Bio-rad) and transferred to a nitrocellulose membrane. After incubation in blocking buffer containing 1X TBS (Tris 20 mM, NaCl 150 mM) and (5% skimmed milk, the membranes were incubated with primary antibodies in blocking buffer at 4°C overnight (anti-HIF-1α (BD Biosciences, clone 54, 1/1000, Le Pont de Claix, France); anti-HIF-2α (Novus Biologicals, 1/400, Noyal Châtillon sur Seiche); anti-HIF-1α (BD Biosciences, clone 29, 1/1000); anti-GLUT-1 (Abcam, 1/1000, Cambridge, UK), anti-β-actin (Sigma-Aldrich, clone AC-15, 1/5000). The membranes were then washed with TBS containing 1% Tween and incubated with secondary antibodies conjugated to HRP (1:5000, Santa Cruz Biotechnology, Dallas, TX). The immunoreactive protein bands were revealed by using the ECL Prime Western Blotting Detection Reagent (Amersham, Amersham, UK) and detected with a ChemiDoc Imaging System (Bio-rad). Densitometry quantification was performed using ImageJ software https://imagej.nih.gov/ (v1.53-j, last accessed March 2021).

Isolation of adipose tissue stroma-vascular fraction

Digestion of fresh PPAT and APAT was performed as previously described [17]. Briefly, adipose tissues were digested with 250 U/ml type I collagenase (Sigma-Aldrich) in PBS containing 2% BSA for 30 min at 37°C, with shaking. After digestion, the cell suspension was filtered through a 250 μm strainer and centrifuged at 300 g for 10 min. Erythrocytes were lysed by incubation at room temperature in erythrocyte lysis buffer (155 mM NH_4Cl, 5.7 mM K2HPO4, 0.1 mM EDTA, pH 7.3) for 10 min followed by successive filtration through 100, 70, and 40 μm strainers. The viable recovered cells were counted and analyzed by flow cytometry.

Flow cytometry analysis

Flow cytometry was performed as initially described with minor modifications [20]. 100 000 stroma-vascular cells were incubated for 30 min at 4 °C in PBS supplemented with 0.5% BSA and 2 mM EDTA containing the fluorescent labeled antibodies: Brilliant Violet 510™ anti-human CD45 Antibody (clone HI30, Biolegend, dilution 1/20), APC anti-human CD206 (clone 19.2, BD Biosciences, dilution 1/10) and PE-Vio 770 anti-human CD14 (clone TÜK4, Miltenyi Biotec, dilution 1/50). As control, a panel of appropriate isotype antibodies was used. The labeled cells were washed with PBS and analyzed in a FACS Canto II flow cytometer using Diva Pro software (BD Biosciences). Cell debris, dead cells and doublets were excluded based on scatter signals. Compensation was established using compensation particles set (BD Biosciences) and single staining and flow cytometer calibration was performed with rainbow calibration particles (BD Biosciences).

ELISA assays

VEGF-A in the conditioned medium from APAT and PPAT samples was quantified by using an ELISA kit (DVE00, R&D Systems, Noyal Châtillon sur Seiche, France) according to the protocol provided by the manufacturer. Optical density was determined at 450 nm using a μQuant microplate reader (Agilent - BioTek instruments, Les Ulis, France). A panel of secreted adipokines were quantified likewise with an ELISA kit (LXSAHM-08; R&D Systems) and a mixture of antibodies against Adiponectin/Acrp30, IL-6, IL-1β, Leptin, PAI-1/ Serpin E1 and TNFα, according to the protocol provided by the manufacturer.

Statistics

Statistical analyses were performed by using GraphPad Prism (v5.04). The univariate relationship between fat measurement and BMI was performed by using Spearman's correlation. Frequency distribution was calculated for fat lobule size and the mean diameter of collagen fibers and two-way ANOVA was performed followed by the Bonferroni post-test. Comparisons between APAT and PPAT were performed using a paired t-test or Mann and Whitney's U test when data are not normally distributed. Comparisons between lean and obese patients were performed using Student's t-test. Normal distribution of the data was determined using the Kolgomorov-Smirnov test. P values < 0.05 (*), < 0.01 (**), and < 0.001 (***) were deemed as significant.

Study approval

The study was conducted in accordance with the guidelines and with the full approval of the national ethics committee (AC-2020-4031). Written informed consent was received from participants prior to inclusion in the study, which was conducted in accordance with the Declaration of Helsinki Principles as revised in 2000.

Results

Differences between PPAT and APAT

To investigate how PPAT might differ from other adipose depots depending on the BMI of the individual, we examined a cohort of 54 patients awaiting prostatectomy for PCa by using pre-operative multi-parametric magnetic resonance imaging (mpMRI) of PPAT, subcutaneous adipose tissue (SAT) and abdominopelvic adipose tissue (APAT; see Figure 1A). Subcutaneous fat thickness at the upper border of the pubic symphysis was used as an indicator of the accumulation of SAT [21]. The volume of the APAT, which is located in front of the bladder and behind the abdominal muscles (Figure 1A), was measured on contiguous axial slices. We chose this fat depot because, like PPAT, it is located in the extra-peritoneal area and can be removed easily during surgery for further biological comparisons. The volume of PPAT was measured on successive slices from the base to the apex of the prostate. Both APAT volume (Figure 1B) and SAT thickness (Figure 1C) correlated with BMI, consistent with a previous study [6]. By contrast, PPAT volume was independent of BMI (Figure 1D), also in accord with several previous studies [6]. These data confirm that PPAT differs from other adipose depots in its regulation by obesity and show that APAT can be used as a control tissue since it behaves like typical adipose tissue.

WAT comprises distinct lobules containing clusters of adipocytes separated from each other by fibrous septa [17]. Upon dissection, the lobules in PPAT were smaller and more numerous than those in APAT (Figure 1E). The weight distribution of the lobules indicated a significantly larger proportion of small lobules (<20 mg) in PPAT when compared with those in APAT (Figure 1F) and the mean lobule weight in PPAT was smaller than in APAT (Figure 1G). Also, the adipocytes in PPAT were slightly smaller than those in APAT (Figure 1H-I). These findings

indicate that the two adipose tissues differ in their organization, with smaller lobules in PPAT when compared to those in APAT.

The microvasculature of PPAT suggests a hypoxic state

To investigate the vasculature of PPAT and compare it with that of APAT, cleared tissues were immunostained with an antibody against the endothelial marker CD31 and visualized the stained tissue by 3D confocal imaging. In WAT, classically, each fat lobule in adipose tissue is supplied by a vascular bundle of arterioles and venules, which, in turn, are subdivided into capillaries that surround individual fat cells [22]. At low magnification, the vascular network of PPAT appeared much less dense than that of APAT (Figure 2A, top panels) and this was more evident at higher magnification and upon 3D reconstruction of the vasculature (Figure 2A, middle and bottom panels). 3D reconstruction of the adipocytes and associated capillaries showed a generally less dense structure in PPAT with capillaries surrounding groups of adipocytes whereas in APAT capillaries tend to surround individual adipocytes (Figure 2A, bottom panels). This distinct organization could be seen also by analyzing representative focal planes from 3D images of APAT and PPAT (Figure 2B) stained with an antibody against CD31 to show endothelial cells (top) and with phalloidin (an actin stain) that delineated the adipocytes (middle). When these images were merged (bottom), in PPAT few adipocytes were seen to contact endothelial cells in contrast to APAT. Quantification of the vascular network after 3D reconstruction showed the total length of the vessel network was significantly smaller in PPAT than in APAT as was the number of branches (Figure 2C and 2D). Similar analyses of PPAT from patients without PCa also found a low-density vasculature in PPAT when compared with APAT (Supplemental Figure S1A). This vascular organization in PPAT suggests that this tissue might be hypoxic.

Transcriptomics reveals a hypoxic signature in PPAT that exhibits an increased expression of HIF-2α

To study the biological consequences of the structure of PPAT, the transcriptomes of paired PPAT and APAT were sequenced. Unsupervised principal component analysis of the whole transcriptome datasets showed that the first dimension, which accounted for 63.5% of the dataset variance, separated samples according to their anatomical location whereas the second dimension, which accounted for 16.1% of dataset variance, discriminated between samples according to the identity of the patient (Figure 3A). These strong differences indicate the specific character of PPAT.

To investigate further the differences between PPAT and APAT, differential gene expression was evaluated using a linear modeling fitted for a small number of samples [23]. Among the 3935 differentially expressed genes we identified, 1479 were upregulated in PPAT, of which 604 were strongly upregulated (i.e. adjusted p-value < 0.01 and fold change > 2), whereas 2456 were downregulated, of which 817 were strongly downregulated (Figure 3B and Supplemental Table S2). Those genes that were considered to be only mildly differentially expressed could discriminate between samples according to their anatomical location, albeit less well than those genes that were strongly differentially expressed (Supplemental Figure S2A–D). To identify key features and a molecular signature specific to PPAT, pathway analysis was performed on the differentially expressed genes by using the Molecular Signatures Database (www.gsea-msigdb.org, last accessed May 28, 2021). Most of the pathways associated with upregulated and downregulated genes were related to the hypoxia response (Figure 3C). A large set of genes that were downregulated are associated with metabolic pathways such as fatty acid metabolism, cholesterol homeostasis and oxidative

phosphorylation; the latter was the most strongly downregulated pathway (Figure 3C). Adipogenesis, which is downregulated in hypoxic adipose tissue [24], was among the pathways downregulated in PPAT when compared with APAT (Figure 3C; see Supplemental Figure S3A for the heatmap with a detailed list of genes). Among the upregulated pathways, the majority were associated with hypoxia (Figure 3C). Single-sample gene set enrichment analysis confirmed the upregulation of genes in the hypoxia pathway (Supplemental Figure S4A) and the positive correlation between hypoxia enrichment scores and other hallmarks upregulated in PPAT (Figure 3C and Supplemental Figure S4B). By contrast, pathways downregulated in PPAT correlated negatively with hypoxia hallmark enrichment scores (Figure 3C and Supplemental Figure S4B). In addition to upregulation of genes related to hypoxia (see Figure 3D for the heatmap with detailed list of genes), genes related to several signaling pathways that are known downstream effectors in hypoxia signaling, including the Beta-CATENIN and NOTCH signaling pathways [25–27], were strongly upregulated in PPAT (Figure 3C). Also, genes related to the inflammatory response and the epithelial-to-mesenchymal transition (including ECM proteins), which are key hallmarks of the hypoxic microenvironment, were upregulated in PPAT (Figure 3C). Together, this unbiased comparison of PPAT and APAT transcriptomes reveals hypoxic traits in PPAT consistent with the low-density vasculature of this tissue.

The cell's response to hypoxia is mediated by two heterodimeric hypoxia-inducible factors (HIFs), which comprise an α subunit (HIF-1α or HIF-2α) whose expression is regulated by oxygen and an oxygen-insensitive β subunit [28]. Hypoxia prevents hydroxylation of the HIFα subunits by prolyl hydroxylases, thereby inhibiting their degradation and promoting HIF-dependent upregulation of genes involved in cell survival, angiogenesis, metabolism, inflammation, the ECM and its remodeling [28]. In normoxic conditions, by contrast, degradation of the HIFα subunits occurs within minutes [28].

If PPAT is indeed a hypoxic tissue, we might expect to find relatively high levels of HIFs in it. To test this prediction, HIF subunits were analyzed in samples of PPAT and APAT that were taken from patients and immediately incubated in lysis buffer in the operating theatre to avoid exposure of the tissue to ambient oxygen, and then rapidly transferred to the research laboratory for protein extraction. Immunoblotting of the protein extracts revealed more HIF-2α in samples of PPAT than in paired APAT samples whereas HIF-1α was undetectable in both tissues (Figure 3E). By contrast, similar amounts of the oxygen-insensitive β-subunit were found in the two tissues (Figure 3F). When the tissue samples were transferred from the operating theatre to research laboratory in culture medium, only the stable HIF-1α subunit was detected by immunoblotting, indicating the importance of immediate lysis of the samples to detect the HIFα subunits (Supplemental Figure S5).

To investigate whether the large amount of HIF-2α in PPAT was associated with an adaptive response to hypoxia, the expression of target genes of HIF-2α involved in metabolism and angiogenesis were harvested. By immunoblotting, there was significantly more of the glucose transporter protein GLUT-1, a HIF target gene product in adipocytes [29], in PPAT than in APAT (Figure 3G). Likewise, as determined by RT-qPCR, there was more *VEGF-A* and *VEGF-B* mRNA in PPAT than in APAT (Figure 3H-I) and, as determined by ELISA, more secreted VEGF-A protein in the conditioned medium of PPAT than in that of APAT (Figure 3I). Thus, consistent with the hypoxic nature of PPAT, we find more HIF-2α and its target gene products in this tissue than in the control APAT.

PPAT displays features of inflammation in lean patients

Accumulating evidence indicates that the chronic hypoxia observed in WAT from obese individuals leads to tissue inflammation, which is characterized by infiltration of immune cells

including macrophages, increased secretion of pro-inflammatory cytokines and decreased secretion of the anti-inflammatory adipokine, adiponectin [24,30], and is tightly associated with interstitial fibrosis [9,24]. The transcriptomics analysis of PPAT found a significant increase in expression of many genes involved in inflammation. The genes related to the inflammatory response hallmark overexpressed in PPAT were also present in the heatmap, which discriminates PPAT from APAT (Figure 4A). To explore further the possibility that the hypoxic state of PPAT might be associated with chronic inflammation, adipose tissue macrophages **in the stroma vascular fractions of PPAT and APAT samples from 25 patients were analyzed by using FACS.** These macrophages are characterized by their expression of the common leukocyte antigen CD45 and the monocyte differentiation antigen CD14. In both PPAT and APAT, $CD45^+$ $CD14^+$ macrophages comprised two populations based on the mannose receptor CD206 expression with CD206+ macrophages, predominant in both ATs as resident macrophages with a remodeling phenotype [31] and CD206- macrophages identified as pro-inflammatory recruited population. The proportion of the pro-inflammatory CD206- macrophages was larger in PPAT than in APAT, whereas there was no significant difference in the proportions of CD206+ macrophages in the two tissues (Figure 4B). The mean concentration of adiponectin was significantly lower in the conditioned medium from PPAT than in that from APAT (Figure 4C) whereas that of leptin was not (Figure 4D). The mean concentrations of pro-inflammatory cytokines TNFα, IL-6 and IL-1β (Figure 4E–G) and plasminogen activator inhibitor (PAI)-1 (Figure 4H), whose expression in adipose tissues is upregulated by inflammation [9,32], were all higher in PPAT than in APAT. Thus, PPAT exhibits hallmarks of chronic inflammation in accordance with its hypoxic state.

Increased amounts of ECM components in PPAT

Fibrosis is one of the hallmarks of adipose tissue hypoxia in obesity [9,24]. Our transcriptomics study showed increased expression of many genes involved in ECM organization in PPAT, consistent with fibrosis. Genes encoding several collagen isoforms, including *COLIA2*, type VI and IV collagens, were more highly expressed in PPAT than in APAT (Figure 5A). Also, genes encoding certain markers of ECM-producing myofibroblasts [33], such as *SNAIL*, or regulators of myofibroblast activation, such as *INHBA* or *GREM1*, were highly expressed in PPAT (Figure 5A). Analysis of the protein–protein interaction network of the products of ECM-related genes that were differentially expressed in PPAT and APAT showed the likely importance of collagen-containing ECM assembly in the differences observed (Figure 5B).

To investigate collagen deposition in PPAT and APAT, sections of paraffin-embedded PPAT and paired APAT samples were stained with Masson's Trichrome, which stains blue the fibrillar collagens [34]. Whereas the staining of APAT showed sparse and thin collagen sheets, the staining of PPAT revealed large areas of staining and fibrotic bundles of various thickness running along the adipose tissue lobules (Figure 5C). Quantification of the staining indicated enhanced collagen deposition in PPAT when compared to APAT (Figure 5C). Together, these data indicate that the ECM is more extensive in PPAT than in APAT.

An obesity-like ECM phenotype in PPAT independent of BMI

The volume of PPAT is independent of BMI, yet ECM gene expression and protein levels are higher in this tissue than in APAT, suggesting obesity-like fibrosis. We hypothesized that, in contrast to APAT, obesity would not further increase the fibrosis seen in PPAT. To investigate this hypothesis, the collagen networks were examined in PPAT and APAT tissues from lean and obese patients by using 3D confocal microscopy followed by reconstruction of the observed collagen fiber network. No difference was observed in this network in PPAT from

lean and obese individuals whereas the network in APAT was substantially more dense in obese patients than it was in lean ones (Figure 6A). The collagen fiber network in PPAT from lean patients, however, was much denser than that in APAT. These conclusions were verified by quantifying the volume of collagen fibers seen in the 3D reconstructions (Figure 6B) and their diameters (Figure 6C) by using Imaris software.

To confirm our finding that obesity has no influence on the collagen content in PPAT, a different approach was used based on quantification of hydroxyproline, a component of collagen that comprises around 13.5% of its amino acid composition [35]. Consistent with the analysis of the collagen fiber network,-significantly more hydroxyproline was found in PPAT than in paired APAT from lean patients; whereas there was more hydroxyproline in APAT from obese patients than in the same tissue from lean patients, but no differences in PPAT from lean and obese patients (Figure 6D). Together, these data confirm that there is more ECM in PPAT than in APAT from non-obese individuals, but the ECM of PPAT in lean and obese individuals resembles that of APAT in obese individuals irrespective of the BMI of the patients.

Discussion

In this study, the characterization of the structural organization of PPAT in humans was set out as a route to understanding more about its biology. Our findings reveal the distinctive tissue organization of PPAT and show, in particular, that it has a sparse vascular network. Consistent with this, PPAT exhibits hallmarks of chronic hypoxia including inflammation and a dense collagen network typical of fibrosis. These features may explain its failure to expand in obese individuals and its contribution to prostate-related disorders.

The present study of a cohort of 54 PCa patients showing that, unlike other adipose depots, the volume of PPAT is independent of BMI, confirms the observations of several previous studies, which used either computerized tomography or MRI to measure PPAT volume [6]. The results in accordance with previous studies [6] reveal that albeit not correlated to BMI PPAT is able to accumulate at various levels since we observed variation in the PPAT volume from 23.77 cm3 to 90.72 cm3. Thus the limited PPAT expandability with BMI is not due to anatomical constraints but rather by active biological processes. A large number of recent studies have demonstrated that there is a correlation with PPAT accumulation and PCa aggressiveness (reviewed in Nassar et al [6]). Characterization of the mechanisms that drive PPAT development independently of BMI remains to be deciphered to explain the role of abundant PPAT in PCa progression. These studies will certainly benefit from the extensive characterization of the structural organization of PPAT presented here. In the present study APAT was used as a control tissue against which to compare PPAT because both adipose tissues are located in the extra-peritoneal area and can be removed easily during surgery. Here, we show that, like other WAT, the volume of APAT correlates with BMI, offering an appropriate control tissue for further studies of PPAT.

Human WAT is highly vascularized and its expansion in obesity depends on its well-defined vascular network structure with each adipocyte surrounded by one or more capillaries [22,36], as we observed in APAT. This close contact between cells and capillaries allows the circulation to provide the nutrients, oxygen, and soluble factors (hormones, growth factors, cytokines) required for tissue homeostasis [36]. By comparison, the vasculature of PPAT is less dense, with fewer capillaries surrounding groups of adipocytes. This atypical organization is most probably the physiological state of the normal PPAT rather than a consequence of its proximity to PCa because we saw a similar vascular organization in PPAT samples from patients devoid

of cancerous lesions in the prostate. Moreover, tumors generally stimulate angiogenesis [37,38], so it is unlikely that the observed decrease in vascularity would be due to secretions from the nearby tumor. The physiological function of this atypical vascular organization is unclear, but may be related to its response to steroid hormones. One study reported that the volume of PPAT is reduced by 5α-reductase inhibitors [39], which inhibit conversion of testosterone into dihydrotestosterone in the prostate gland and also decrease the volume of the prostate due to apoptosis of epithelial cells [40]. Consistent with this idea, androgen- and estrogen-responsive genes are upregulated in PPAT when compared to those in APAT. Sex hormones influence the metabolism, endocrine functions and angiogenesis of certain other adipose tissues [41,42], so these findings raise the interesting possibility that they might also influence PPAT physiology and development, an avenue that deserves further investigation.

The unusual organization of the vasculature in PPAT led us to postulate that this tissue might be hypoxic. Unbiased comparison of PPAT and APAT transcriptomes indeed revealed a hypoxic signature in PPAT: most of the biological pathways relevant to hypoxia are differentially represented in the transcriptome of PPAT when compared with that of APAT. Moreover, there is a specific increase in expression of the oxygen-labile HIF-2α, but not of HIF-1α, in PPAT, indicating an adaptive response of this tissue to hypoxia. Both HIF-1α and HIF-2α form heterodimers with the constitutive HIF-1β subunit to form the transcription factors HIF-1 and HIF-2, which both mediate the hypoxic response [28]. Although HIF-1 and HIF-2 have common target genes, such as *VEGFA* and *GLUT1*, they also have specific target genes, depending on the tissue, as well as differences in their temporal regulation [43]. These differences might explain why HIF-2α, but not HIF-1α, is overexpressed in PPAT and the consequences of its overexpression in this tissue. Indeed, in some systems HIF-1 α drives the initial response to hypoxia whereas chronic hypoxia involves HIF-2 α [43–45]. In addition, HIF-2 is active under

mild hypoxia (< 5% O_2) with a long lasting response whereas HIF-1 is most active during short periods of intense hypoxia or anoxia (< 0.1%) [43,45]. This distinct temporal regulation might explain why HIF-2 overexpression occurs in PPAT, which is likely to exhibit chronic mild hypoxia. The importance of chronic HIF-2α overexpression in adipose tissue inflammation is illustrated by mice with an adipose tissue-specific deletion of the gene encoding Von Hippel–Lindau (VHL) protein, which is required for degradation of both HIF-1α and HIF-2α by the proteasome [28]. In these mice, chronic activation of HIFs causes adipose tissue inflammation characterized by overexpression of pro-inflammatory cytokines, such as IL-6 and TNF-α, and chemokines [46]. Genetic deletion of *HIF-2α*, but not *HIF-1α*, abrogates this inflammation, demonstrating that this isoform is key to the inflammatory response of adipose tissue to chronic hypoxia [46]. Consistent with the findings from the *VHL* gene knockout mice, we observed downregulation of the anti-inflammatory adipokine adiponectin [30] in PPAT and overexpression of the pro-inflammatory cytokines IL-6, TNF-α and IL1-β. Like inflammation, enhanced ECM deposition, or fibrosis, is a hallmark of the hypoxic response in adipose tissue [47,48]. To our knowledge, the role specifically of HIF-2α in the induction of fibrosis in hypoxic adipose has not been investigated, but studies have shown that HIF-2 can induce transcription of genes encoding ECM components leading to fibrosis in the liver [49] and lungs [50].

The higher level of VEGF secretion by PPAT when compared to APAT might be expected to promote angiogenesis; apparently, however, it is not sufficient to counteract the hypoxic state of PPAT. This might be due to the lower level of adiponectin secreted by PPAT as well as the overexpression of PAI-1 when compared to APAT, which have been shown to inhibit new vessel formation and may counterbalance any VEGF-induced angiogenesis [51]. A resulting suboptimal level of angiogenesis might be sufficient to limit the dysfunctional state of PPAT but not to resolve hypoxia.

In addition to explaining the high basal inflammatory state of PPAT, our findings also provide a likely explanation why PPAT does not expand in obesity: the extensive ECM and fibrosis we see in this tissue may prevent any expansion of PPAT in obese individuals. Previous studies of human and rodent adipose tissues shows that fibrosis alters the plasticity of the tissue and places a physical constraint on its expansion [48,52]. We find that obesity causes no increase in ECM deposition in PPAT beyond that seen in the PPAT of lean individuals, but the ECM of PPAT resembles that of WAT in obesity. We propose that this obesity-like organization of the ECM in PPAT does not adapt to external signals, but provides an important physical constraint on PPAT expansion. A recent study demonstrated that obesity was not associated with adipocyte hypertrophy in PPAT [53], consistent with the idea that PPAT is in a state of maximum expandability in lean individuals. Moreover, we found that the genes related to adipogenesis are downregulated in PPAT as compared to APAT, which might also contribute to its failure to expand during obesity. The basal inflammatory state of PPAT might also contribute to the inability of this tissue to expand during obesity because inflammation of adipose tissue contributes to perpetuating fibrosis [48,54] and also interferes with adipocyte differentiation [55,56], which may explain the inhibition of adipogenesis.

The present study opens new mechanistic avenues to explain the role of PPAT in prostate disorders. First, the hallmarks of PPAT identified in this study might favor BPH and related lower urinary tract symptoms. In fact, chronic inflammation as well as fibrosis have been associated to this frequent disorder [57]**. The etiology of this chronic inflammation is probably multifactorial but our study highlights that PPAT needs to be considered as an important contributor of this process as also proposed by a recent review [15]. Regarding PCa**, clinical studies have already established evidence of a link between PPAT inflammation, independent of obesity, and the occurrence of high grade PCa [10–12]. There is accumulating evidence that pro-

inflammatory cytokines contribute through multiple signal transduction pathways to PCa initiation and in established tumors to growth, survival, metastasis and resistance to therapy [58]. Our study deciphers the mechanism by which PPAT is an important source of pro-inflammatory molecules that might promote PCa initiation and progression. The present work highlights that PPAT might also contribute to PCa progression through fibrosis. In fact, the large amounts of ECM in PPAT might directly affect tumor progression by increasing ECM stiffness, which in proximal mammary adipose tissue has been found to promote mammary tumor progression *in vivo* [59,60]. In addition, these changes in ECM might promote tumor progression directly by ECM components functioning as signaling molecules. In breast cancer, for example, a bioactive fragment of adipocyte-derived COLVI, called endotrophin, contributes to tumor progression [61]. The consequences of these biological features including the biomechanical specificities in the ECM of PPAT open a new avenue to explain the role of PPAT in prostate-related disorders that deserves further investigation. All the data reported here, and the remaining questions are summarized in Figure 7.

Author Contributions

Conducting experiments and acquiring data: MR, DE, CM, AT, JG, CB, YYJ, CH, SP, SL, DM; Analyzing data: MR, DE, CM, AT, JG, CB, YYJ, CH, SP, PV, MC, JFT, BM, AB, DM, CM ; Designing research studies: MR, DE, AT, JG, AB, DM and CM; Writing of the manuscript: MR, DE, DM, CM; Editing of the manuscript: DE, AT, JG, PV, MC, JFT, BM, AB; Supervision of the study: DM and CM.

Acknowledgements

This work benefited from the Toulouse Réseau Imagerie (TRI)-RIO Optical Imaging Platform at the Institute of Pharmacology and Structural Biology (Genotoul, Toulouse, France). Sequencing was performed by the GenomEast platform, a member of the 'France Génomique' consortium (ANR-10-INBS-0009). We acknowledge Life Science Editors for professional scientific editing during the preparation of the manuscript.

References

1. Zwick RK, Guerrero-Juarez CF, Horsley V, Plikus M V.: Anatomical, Physiological, and Functional Diversity of Adipose Tissue. Cell Metab., 2018, pp. 68–83.
2. Tchkonia T, Thomou T, Zhu Y, Karagiannides I, Pothoulakis C, Jensen MD, Kirkland JL: Mechanisms and metabolic implications of regional differences among fat depots. Cell Metab. 2013, pp. 644–656.
3. Wang YY, Lehuédé C, Laurent V, Dirat B, Dauvillier S, Bochet L, Le Gonidec S, Escourrou G, Valet P, Muller C: Adipose tissue and breast epithelial cells: A dangerous dynamic duo in breast cancer. Cancer Lett., 2012, pp. 142–151.
4. Estève D, Roumiguié M, Manceau C, Milhas D, Muller C: Periprostatic adipose tissue: A heavy player in prostate cancer progression. Curr. Opin. Endocr. Metab. Res., pp. 29–35.
5. Ishidoya S, Endoh M, Nakagawa H, Saito S, Arai Y: Novel Anatomical Findings of the Prostatic Gland and the Surrounding Capsular Structures in the Normal Prostate. Tohoku J. Exp. Med. 2007, 212:55-62.
6. Nassar ZD, Aref AT, Miladinovic D, Mah CY, Raj G V, Hoy AJ, Butler LM: Peri-prostatic adipose tissue: the metabolic microenvironment of prostate cancer. BJU Int., 2018, pp. 9–21.
7. Bandini M, Gandaglia G, Briganti A: Obesity and prostate cancer. Curr. Opin. Urol., 2017, pp. 415–421.
8. Gucalp A, Iyengar NM, Zhou XK, Giri DD, Falcone DJ, Wang H, Williams S, Krasne MD, Yaghnam I, Kunzel B, Morris PG, Jones LW, Pollak M, Laudone VP, Hudis CA, Scher HI, Scardino PT, Eastham JA, Dannenberg AJ: Periprostatic adipose inflammation is associated with high-grade prostate cancer. Prostate Cancer Prostatic Dis, 2017, 20:418–423.
9. Kahn CR, Wang G, Lee KY: Altered adipose tissue and adipocyte function in the pathogenesis of metabolic syndrome. J. Clin. Invest., 2019, pp. 3990–4000.
10. Zhang Q, Sun L jiang, Yang Z gang, Zhang G ming, Huo R cha: Influence of adipocytokines in periprostatic adipose tissue on prostate cancer aggressiveness. Cytokine, 2016, 85:148–156.
11. Finley DS, Calvert VS, Inokuchi J, Lau A, Narula N, Petricoin EF, Zaldivar F, Santos R, Tyson DR, Ornstein DK: Periprostatic Adipose Tissue as a Modulator of Prostate Cancer Aggressiveness. J Urol 2009, 182:1621–1627.
12. Dahran N, Szewczyk-Bieda M, Vinnicombe S, Fleming S, Nabi G: Periprostatic fat adipokine expression is correlated with prostate cancer aggressiveness in men undergoing radical prostatectomy for clinically localized disease. BJU Int, 2019, 123:985–994.
13. Laurent V, Guérard A, Mazerolles C, Le Gonidec S, Toulet A, Nieto L, Zaidi F, Majed B, Garandeau D, Socrier Y, Golzio M, Cadoudal T, Chaoui K, Dray C, Monsarrat B, Schiltz O, Wang YY, Couderc B, Valet P, Malavaud B, Muller C:

Periprostatic adipocytes act as a driving force for prostate cancer progression in obesity. Nat Commun, 2016, 7.
14. Laurent V, Toulet A, Attané C, Milhas D, Dauvillier S, Zaidi F, Clement E, Cinato M, Le Gonidec S, Guérard A, Lehuédé C, Garandeau D, Nieto L, Renaud-Gabardos E, Prats AC, Valet P, Malavaud B, Muller C: Periprostatic adipose tissue favors prostate cancer cell invasion in an obesity-dependent manner: Role of oxidative stress. Mol Cancer Res, 2019, 17:821–835.
15. Passos GR, Ghezzi AC, Antunes E, de Oliveira MG, Mónica FZ: The Role of Periprostatic Adipose Tissue on Prostate Function in Vascular-Related Disorders. Front. Pharmacol., 2021, .
16. Vaysse C, Lomo J, Garred O, Fjeldheim F, Lofteroed T, Schlichting E, McTiernan A, Frydenberg H, Husoy A, Lundgren S, Fagerland MW, Richardsen E, Wist EA, Muller C, Thune I: Inflammation of mammary adipose tissue occurs in overweight and obese patients exhibiting early-stage breast cancer. npj Breast Cancer, 2017, 3.
17. Estève D, Boulet N, Belles C, Zakaroff-Girard A, Decaunes P, Briot A, Veeranagouda Y, Didier M, Remaury A, Guillemot JC, Ledoux S, Dani C, Bouloumié A, Galitzky J: Lobular architecture of human adipose tissue defines the niche and fate of progenitor cells. Nat Commun, 2019, 10.
18. Dobin A, Davis CA, Schlesinger F, Drenkow J, Zaleski C, Jha S, Batut P, Chaisson M, Gingeras TR: STAR: Ultrafast universal RNA-seq aligner. Bioinformatics 2013, 29:15–21.
19. Gilleron J, Méziat C, Sulen A, Ivanov S, Jager J, Estève D, Muller C, Tanti J-F, Cormont M: Exploring Adipose Tissue Structure by Methylsalicylate Clearing and 3D Imaging. J Vis exp, 2020, p. 162.
20. Curat CA, Miranville A, Sengene C, Diehl M, Tonus C, Busse R, Bouloumie A: From Blood Monocytes to Adipose Tissue–Resident Macrophages. Diabetes, 2004, 53.
21. Wang H, Chen YE, Eitzman DT: Imaging body fat techniques and cardiometabolic implications. Arterioscler Thromb Vasc Biol, 2014, 34:2217–2223.
22. Wassermann F: The development of adipose tissue-Compr Physiol Supplement 15: Handbook of Physiology. 1965.
23. Ritchie ME, Phipson B, Wu D, Hu Y, Law CW, Shi W, Smyth GK: Limma powers differential expression analyses for RNA-sequencing and microarray studies. Nucleic Acids Res, 2015, 43:e47.
24. Trayhurn P: Hypoxia and Adipose Tissue Function and Dysfunction in Obesity. Physiol Rev 2013, 93:1–21.
25. Park YK, Park B, Lee S, Choi K, Moon Y, Park H: Hypoxia-inducible factor-2α-dependent hypoxic induction of Wnt10b expression in adipogenic cells. J Biol Chem 2013, 288:26311–26322.
26. Marignol L, Rivera-Figueroa K, Lynch T, Hollywood D: Hypoxia, notch signalling, and prostate cancer. Nat. Rev. Urol. 2013, pp. 405–413.

27. Skuli N, Majmundar AJ, Krock BL, Mesquita RC, Mathew LK, Quinn ZL, Runge A, Liu L, Kim MN, Liang J, Schenkel S, Yodh AG, Keith B, Simon MC: Endothelial HIF-2α regulates murine pathological angiogenesis and revascularization processes. J Clin Invest 2012, 122:1427–1443.
28. Lee P, Chandel NS, Simon MC: Cellular adaptation to hypoxia through hypoxia inducible factors and beyond. Nat. Rev. Mol. Cell Biol., 2020, pp. 268–283.
29. Wood IS, Wang B, Lorente-Cebrián S, Trayhurn P: Hypoxia increases expression of selective facilitative glucose transporters (GLUT) and 2-deoxy-d-glucose uptake in human adipocytes. Biochem Biophys Res Commun 2007, 361:468–473.
30. Ohashi K, Shibata R, Murohara T, Ouchi N: Role of anti-inflammatory adipokines in obesity-related diseases. Trends Endocrinol. Metab., 2014, pp. 348–355.
31. Bourlier V, Zakaroff-Girard A, Miranville A, De Barros S, Maumus M, Sengenes C, Galitzky J, Lafontan M, Karpe F, Frayn KN, Bouloumié A: Remodeling phenotype of human subcutaneous adipose tissue macrophages. Circulation 2008, 117:806–815.
32. Kaji H: Adipose tissue-derived plasminogen activator inhibitor-1 function and regulation. Compr Physiol, 2016, 6:1873–1896.
33. Bourlier V, Sengenès C, Zakaroff-Girard A, Decaunes P, Wdziekonski B, Galitzky J, Villageois P, Esteve D, Chiotasso P, Dani C, Bouloumié A: TGFbeta family members are key mediators in the induction of myofibroblast phenotype of human adipose tissue progenitor cells by macrophages. PLoS One 2012, 7.
34. Halberg N, Khan T, Trujillo ME, Wernstedt-Asterholm I, Attie AD, Sherwani S, Wang Z V., Landskroner-Eiger S, Dineen S, Magalang UJ, Brekken RA, Scherer PE: Hypoxia-Inducible Factor 1α Induces Fibrosis and Insulin Resistance in White Adipose Tissue. Mol Cell Biol, 2009, 29:4467–4483.
35. Neuman RE, Logan MA: The determination of hydroxyproline. J Biol Chem, 1950, 184:299–306.
36. Christiaens V, Lijnen HR: Angiogenesis and development of adipose tissue. Mol. Cell. Endocrinol. 2010, pp. 2–9.
37. Judah Folkman: Tumor angiogenesis: Therapeutic implications. N Engl J Med 1971AD, :1182–1186.
38. Kerbel RS: Tumor Angiogenesis. N Engl J Med 2008, 358:2039–2049.
39. Taussky D, Barkati M, Campeau S, Zerouali K, Nadiri A, Saad F, Delouya G: Changes in periprostatic adipose tissue induced by 5α-reductase inhibitors. Andrology, 2017, 5:511–515.
40. Bass R, Perry B, Langenstroer P, Thrasher JB, Dennis KL, Tawfik O, Holzbeierlein J: Effects of Short-Term Finasteride on Apoptotic Factors and Androgen Receptors in Prostate Cancer Cells. J Urol 2009, 181:615–620.
41. Karastergiou K, Smith SR, Greenberg AS, Fried SK: Sex differences in human

adipose tissues - The biology of pear shape. Biol. Sex Differ. 2012, .
42. Volat F, Bouloumié A: Steroid hormones and the stroma-vascular cells of the adipose tissue. Horm Mol Biol Clin Investig, 2013, 15:5–10.
43. Koh MY, Powis G: Passing the baton: The HIF switch. Trends Biochem. Sci. 2012, pp. 364–372.
44. Koh MY, Lemos R, Liu X, Powis G: The hypoxia-associated factor switches cells from HIF-1α- to HIF-2α-dependent signaling promoting stem cell characteristics, aggressive tumor growth and invasion. Cancer Res 2011, 71:4015–4027.
45. Holmquist-Mengelbier L, Fredlund E, Löfstedt T, Noguera R, Navarro S, Nilsson H, Pietras A, Vallon-Christersson J, Borg Å, Gradin K, Poellinger L, Påhlman S: Recruitment of HIF-1α and HIF-2α to common target genes is differentially regulated in neuroblastoma: HIF-2α promotes an aggressive phenotype. Cancer Cell, 2006, 10:413–423.
46. Lin Q, Huang Y, Booth CJ, Haase VH, Johnson RS, Celeste Simon M, Giordano FJ, Yun Z: Activation of hypoxia-inducible factor-2 in adipocytes results in pathological cardiac hypertrophy. J Am Heart Assoc 2013, 2.
47. Marcelin G, Silveira ALM, Martins LB, Ferreira AVM, Clément K: Deciphering the cellular interplays underlying obesityinduced adipose tissue fibrosis. J. Clin. Invest., 2019, pp. 4032–4040.
48. Sun K, Tordjman J, Clément K, Scherer PE: Fibrosis and adipose tissue dysfunction. Cell Metab., 2013, pp. 470–477.
49. Qu A, Taylor M, Xue X, Matsubara T, Metzger D, Chambon P, Gonzalez FJ, Shah YM: Hypoxia-inducible transcription factor 2α promotes steatohepatitis through augmenting lipid accumulation, inflammation, and fibrosis. Hepatology. 2011, pp. 472–483.
50. Shimoda LA, Semenza GL: HIF and the lung: Role of hypoxia-inducible factors in pulmonary development and disease. Am. J. Respir. Crit. Care Med. 2011, pp. 152–156.
51. Clair Crewe, Yu Aaron An PES: The ominous triad of adipose tissue dysfunction: inflammation, fibrosis, and impaired angiogenesis. J Clin Invest 2017, 7.
52. Khan T, Muise ES, Iyengar P, Wang Z V., Chandalia M, Abate N, Zhang BB, Bonaldo P, Chua S, Scherer PE: Metabolic Dysregulation and Adipose Tissue Fibrosis: Role of Collagen VI. Mol Cell Biol, 2009, 29:1575–1591.
53. Miladinovic D, Cusick T, Mahon KL, Haynes AM, Cortie CH, Meyer BJ, Stricker PD, Wittert GA, Butler LM, Horvath LG, Hoy AJ: Assessment of periprostatic and subcutaneous adipose tissue lipolysis and adipocyte size from men with localized prostate cancer. Cancers (Basel), 2020, 12.
54. Crewe C, An YA, Scherer PE: The ominous triad of adipose tissue dysfunction: Inflammation, fibrosis, and impaired angiogenesis. J. Clin. Invest., 2017, pp. 74–82.
55. Estève D, Boulet N, Volat F, Zakaroff-Girard A, Ledoux S, Coupaye M,

Decaunes P, Belles C, Gaits-Iacovoni F, Iacovoni JS, Rémaury A, Castel B, Ferrara P, Heymes C, Lafontan M, Bouloumié A, Galitzky J: Human white and brite adipogenesis is supported by msca1 and is impaired by immune cells. Stem Cells, 2015, 33:1277–1291.

56. Hammarstedt A, Gogg S, Hedjazifar S, Nerstedt A, Smith U: Impaired adipogenesis and dysfunctional adipose tissue in human hypertrophic obesity. Physiol Rev 2018, 98:1911–1941.
57. Bushman WA, Jerde TJ: The role of prostate inflammation and fibrosis in lower urinary tract symptoms. Am J Physiol Ren Physiol 2016, 311:817–821.
58. Archer M, Dogra N, Kyprianou N: Inflammation as a driver of prostate cancer metastasis and therapeutic resistance. Cancers (Basel)., 2020, pp. 1–24.
59. Iyengar P, Espina V, Williams TW, Lin Y, Berry D, Jelicks LA, Lee H, Temple K, Graves R, Pollard J, Chopra N, Russell RG, Sasisekharan R, Trock BJ, Lippman M, Calvert VS, Petricoin EF, Liotta L, Dadachova E, Pestell RG, Lisanti MP, Bonaldo P, Scherer PE: Adipocyte-derived collagen VI affects early mammary tumor progression in vivo, demonstrating a critical interaction in the tumor/stroma microenvironment. J Clin Invest, 2005, 115:1163–1176.
60. Seo BR, Bhardwaj P, Choi S, Gonzalez J, Eguiluz RCA, Wang K, Mohanan S, Morris PG, Du B, Zhou XK, Vahdat LT, Verma A, Elemento O, Hudis CA, Williams RM, Gourdon D, Dannenberg AJ, Fischbach C: Obesity-dependent changes in interstitial ECM mechanics promote breast tumorigenesis. Sci Transl Med, 2015, 7.
61. Park J, Scherer PE: Adipocyte-derived endotrophin promotes malignant tumor progression. J Clin Invest 2012, 122:4243–4256.

Figure legends

Figure 1. The accumulation of PPAT is independent of BMI and its morphology differs from APAT (A) Sagittal (left panel) and axial (right panel) sections of the midbody of a man as seen by T2-weighted MRI. The locations of PPAT, APAT and SAT. Dotted lines on sagittal section indicate the position of axial sections represented. P: Prostate **(B–D)** Correlations between the BMI of each patient and APAT volume (n=54) **(B)**, SAT thickness (n=40), and **(C)** PPAT volume (n=56) **(D)**. **(E)** Representative images of the size of the lobules obtained after dissection of the indicated amounts of APAT and PPAT (scale in cm). **(F)** Lobule weight distribution in paired PPAT and APAT samples (n= 10). **(G)** Mean lobule weight in paired APAT and PPAT samples (n= 10). **(H)** Representative images of HE stained, paraffin-embedded APAT and PPAT tissue sections. Scale bars, 500 μm. **(I)** Mean diameter of adipocytes in paired APAT and PPAT tissue sections as in **(H)** (n=18). Correlation coefficients and p-values were calculated by using Spearman's correlation. Bars indicate mean ± SEM; statistical significance was determined by two-way ANOVA followed by Bonferoni post-test, †††† $p<0.0001$ (F), and by paired Student's t-test *$p < 0.05$, **$p < 0.01$ (G and I).

Figure 2. The microvasculature of PPAT suggests a hypoxic state. (A) Representative z stack confocal images of cleared PPAT and APAT stained with anti-CD31 showing the capillary networks (upper panels: scale bars, 300 μm). The zones indicated by the dotted squares are shown in higher magnification (ZOOM) in the images below (scale bars, 50 μm). 3D reconstructions of the microvasculature (gray) and adipocytes (randomly color coded to identify each adipocyte) were made using Imaris software. **(B)** A representative single focal plane (thickness 8 μm) extracted from 3D confocal images of paired APAT and PPAT samples stained with anti-CD31 (magenta, upper panel), phalloidin (green, middle panel) and the merge images (lower panel; scale bars, 50 μm. **(C and D).** Quantification after 3D reconstruction of the total length of the vessels **(C)** and the number of branches **(D)** in APAT (n=7) and PPAT (n=5). Bars represent means ± SEM; statistical significance was determined by paired Student's t-test, *$p < 0.05$, **$p < 0.01$.

Figure 3. Transcriptomics reveals a hypoxic signature in PPAT associated with an increased expression of HIF-2α. (A) Principal component analysis performed on the whole

transcriptomics dataset. Ellipses represented the confidence interval for the PPAT group and the APAT (n=3 per group, Upper panel). Volcano plot representing the average log2 fold change (PPAT/APAT) versus –log10 p-value (n=3 per group, lower panel). Vertical dotted lines indicate the limits for genes that are 2-fold over or under represented (i.e. log2 fold-change above 1 or below -1 respectively). Horizontal dotted line indicated genes that reach the cut off p-value ($p < 0.05$). Dark blue dots show highly under-represented (i.e. strong downregulation) genes (i.e. adjusted p value < 0.01 and log2 fold change < -1). Light blue dots show mildly under-represented (i.e. mild downregulation) genes (i.e. p value < 0.05 and log2 fold change < -1). Dark red dots show highly over-represented (i.e. strong upregulation) genes (i.e. adjusted p value < 0.01 and log2 fold change > 1). Light red dots show mildly over-represented (i.e. mild upregulation) genes (i.e. p value < 0.05 and log2 fold change > 1). **(B)** Balloon plots representing the pathways enriched in each gene category according to the hallmark collection in the Molecular Signatures database. The size of each balloon is setup according to the percentage of genes belonging to each pathway enriched and the color according to –log10 of the q-value. Relationship between hypoxia hallmark and other enriched hallmarks was evaluated as Pearson correlation of enrichment score determined with the Single-sample Gene Set Enrichment Analysis algorithm. **(C)** Heatmap and hierarchical clustering of sample based on upregulated genes belonging to the hypoxia hallmark (n=6). **(D)** Representative western blots of HIF-1α, HIF-2α and β-actin in paired samples of PPAT and APAT (upper panel) and quantification of HIF-2α (n=4) (lower panel). **(E)** Representative western blots of HIF-1β and β-actin in paired samples of PPAT and APAT (upper panel) and quantification (n=8) (lower panel). **(F)** Representative western blots of GLUT-1 and β-actin in paired samples of PPAT and APAT (upper panel) and quantification (n=8) (lower panel). In **(D-F)**, PC-3 cells treated or not with $CoCl_2$ were used as controls. **(G, H)** *VEGF-A* **(G)** and *VEGF-B* **(H)** mRNA expression were determined by RT-qPCR in paired samples of PPAT and APAT (n= 6)**. (I)** Secreted VEGF-A was measured by ELISA in conditioned media from paired samples of PPAT and APAT (n=19)**.** Bars indicate means ± SEM. Statistical significance was determined by Student's t-test: *$p < 0.05$; ** $p < 0.001$.

Figure 4. PPAT displays features of inflammation in lean patients. (A) Heatmap and hierarchical clustering of PPAT and APAT samples based on upregulated genes belonging to

the inflammatory response hallmark (n=6). **(B)** Quantification of resident macrophages (CD206+) and recruited monocytes (CD206-) in the CD45+/CD14+ population in the stroma vascular fractions of paired PPAT and APAT samples (n=25)**.** (**C–H**) Adiponectin/Acrp30 (n=10) **(C)**, leptin (n=10) **(D)**, TNF-α (n=10) **(E)**, IL-6 (n=8) **(F)**, IL-1β (n=10) **(G)** and PAI-1 (n=10) **(H)** in conditioned media from paired PPAT and APAT samples were quantified by ELISA. Bars indicate means ± SEM. Statistical significance was determined by Mann and Whitney's U test (B), † $p < 0.05$**,** and paired Student's t-test (C–H), * $p < 0.05$.

Figure 5. Increased amounts of ECM components in PPAT from lean patients. **(A)** Heatmap and hierarchical clustering of PPAT and APAT samples based on upregulated genes belonging to the EMT hallmark (n=6). **(B)** Protein–protein interaction network showing the relationship of genes upregulated in the EMT to the biological processes as indicated by gene ontology analysis. Clear circles indicate genes and brown circles indicate biological processes. Edges indicate interactions with a confidence score above 0.7. **(C)** Representative images of paraffin-embedded tissue sections of paired APAT and PPAT samples after Masson's Trichrome stain (left panels, scale bars 500μm) and the zones indicated by the dotted squares are shown in higher magnification zoom (right panels; scale bars, 100 μm). Quantification of staining (right panel) was performed on whole tissue sections (n=19). Statistical significance was determined by Student's t-test, * $p < 0.05$.

Figure 6. An obesity-like ECM phenotype in PPAT independent of BMI. (A) Representative 3D confocal images of Picrosirius Red staining (left panel) and 3D reconstruction of collagen fibers (right panel) in paired APAT and PPAT samples from lean (mean BMI = 24.5 ± 0. 6 kg/m^2, mean age = 65.4 ± 2.2 years) and obese (mean BMI = 32.4 ± 1.2 kg/m^2, mean age = 66.2 ± 2.2 years) patients. Reconstructed collagen fibers are color-coded according to their mean diameter as shown below. Scale bars, 50μm. **(B)** Quantification of collagen fiber volume in Picrosirius Red-stained paired APAT and PPAT samples from lean (n=6) and obese patients (n=6). **(C)** Distribution of the number of collagen segments according to their diameter measured after 3D reconstruction in paired APAT and PPAT samples from lean (n=6) and obese patients (n=6). Two-way ANOVA analysis retrieved $p < 0.001$. **(D)** Hydroxyproline concentrations in paired APAT and PPAT samples from lean (n=9) and obese patients (n=10).

Bars indicate means ± SEM. Statistical significance was determined by Student's t-test, * $p < 0.05$.

Figure 7. The chronic hypoxic state of PPAT limits its expansion in obesity and favors tumor progression. PPAT has an atypical vascular organization when compared to other adipose tissues, with a sparse vascular network surrounding clusters of adipocytes rather than individual cells. In our working model, this contributes to a chronic hypoxic state leading to the overexpression of HIF-2α. In accord with its hypoxic state, PPAT exhibits hallmarks of chronic inflammation such as the presence of pro-inflammatory macrophages, increased secretion of pro-inflammatory cytokines and decreased secretion of the anti-inflammatory adipokine, adiponectin. Also, PPAT has more ECM and, specifically, more collagen, another hallmark of hypoxia. This chronic hypoxic state in PPAT probably limits its expansion in obese individuals and results in features known to favor prostate-related disorders.

Figure 1

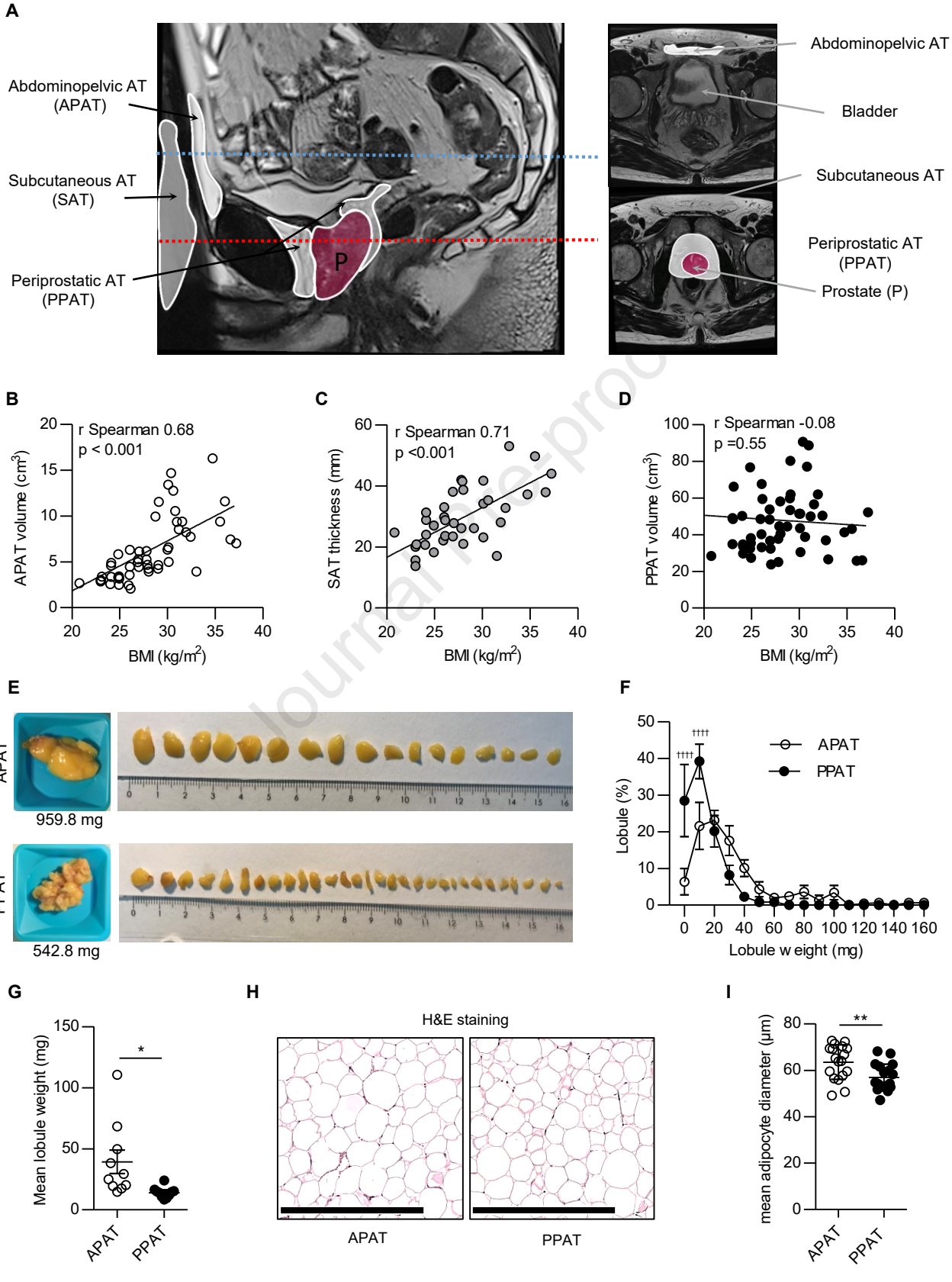

Figure 2

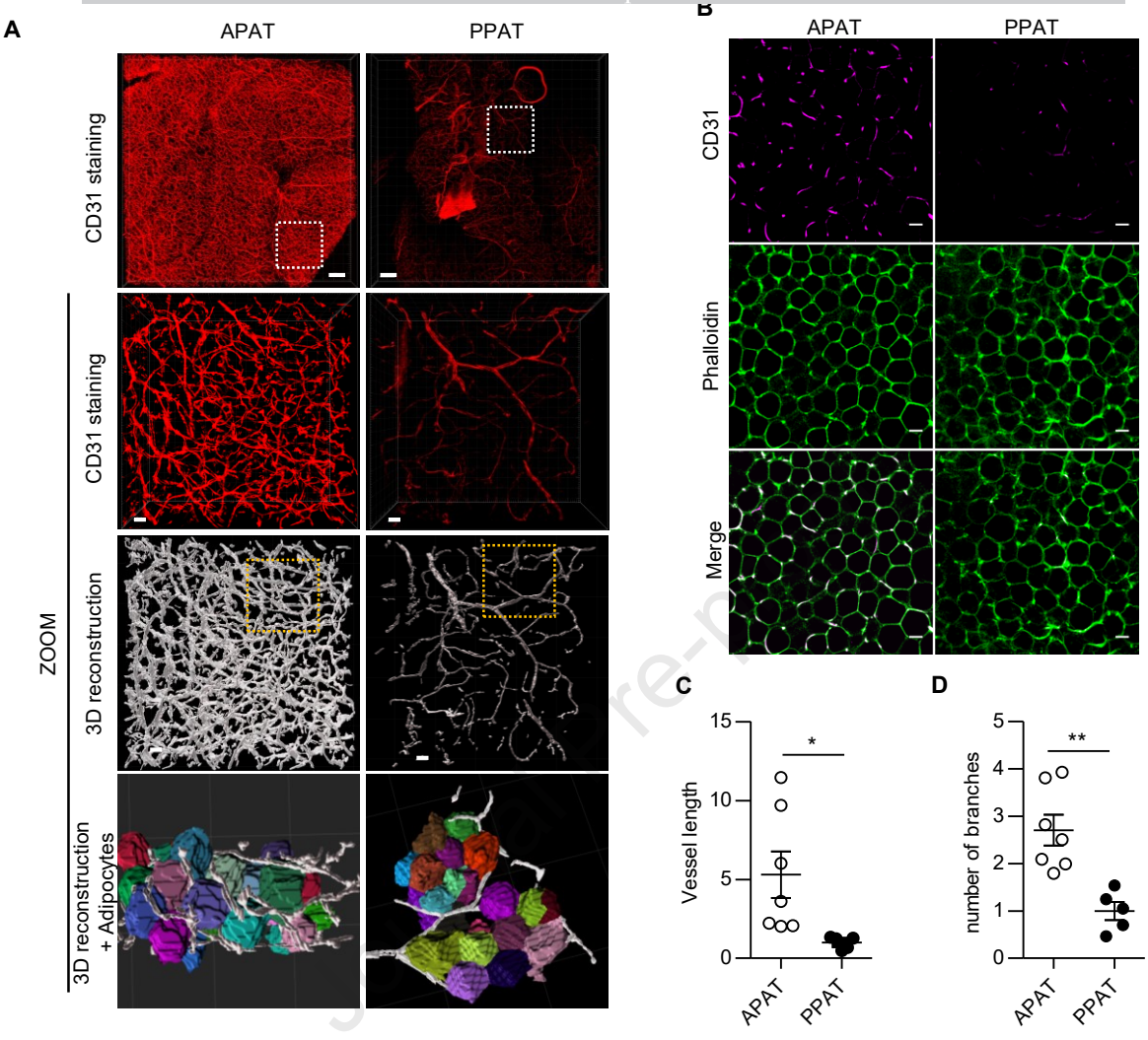

Figure 3

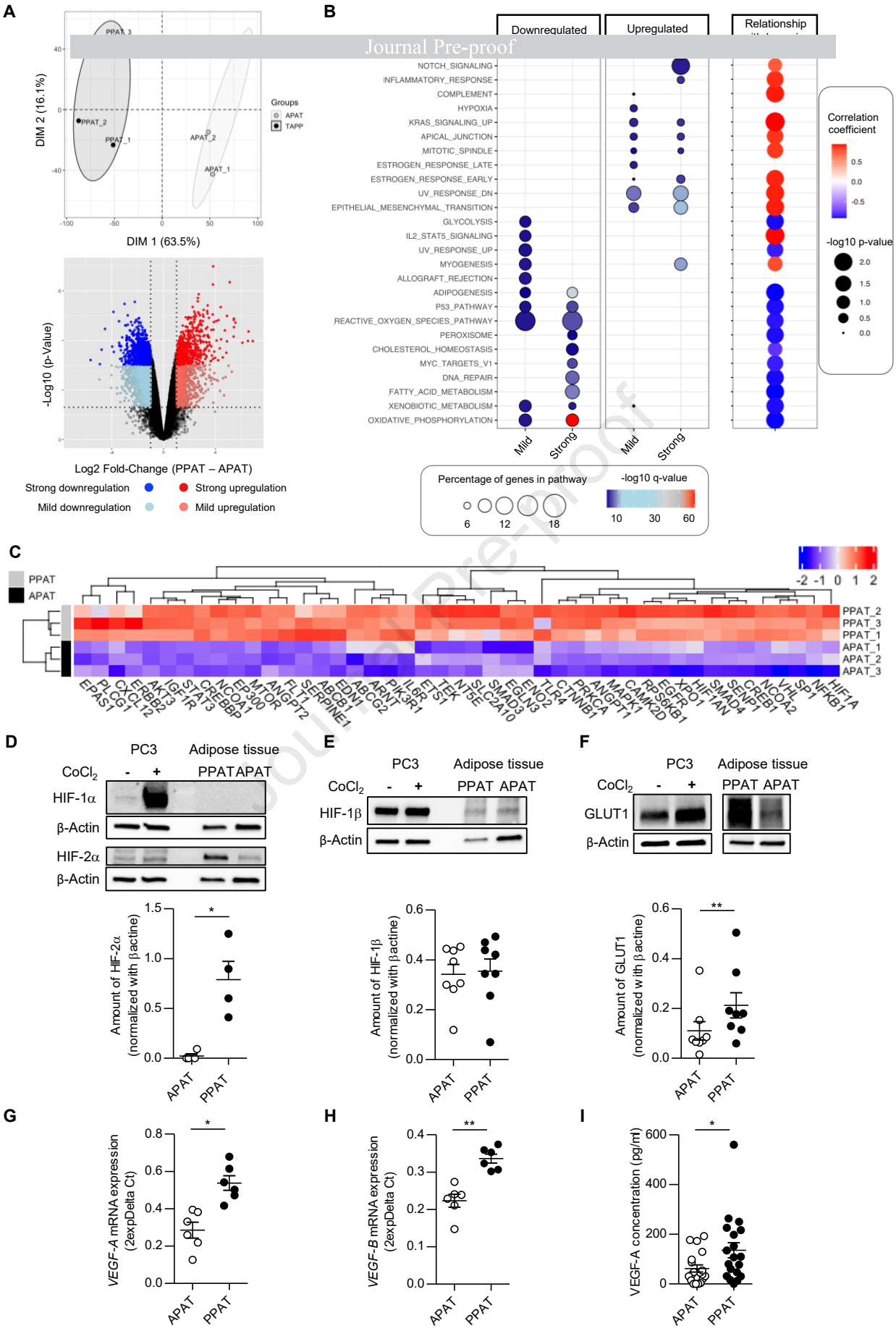

Figure 4

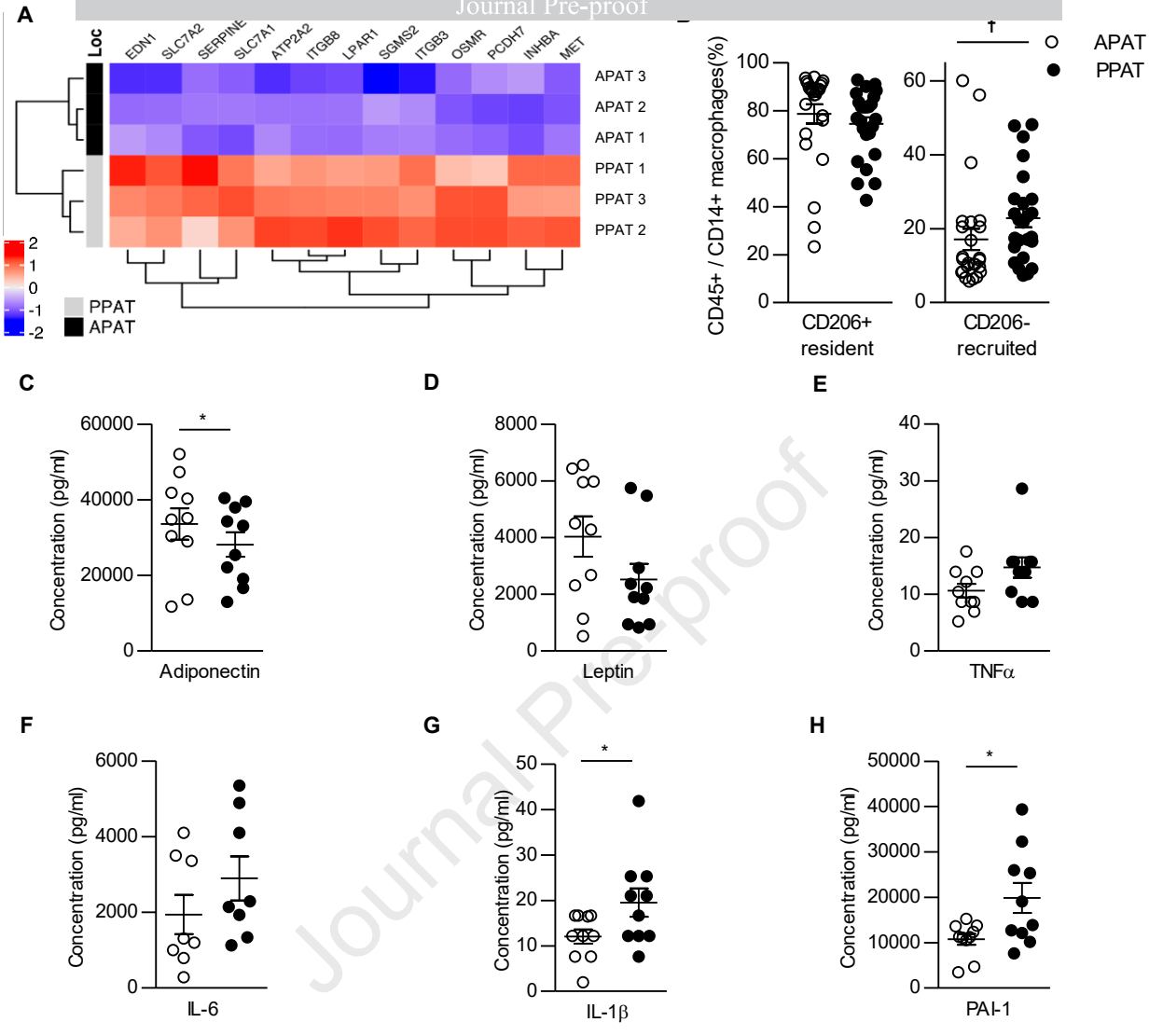

Figu

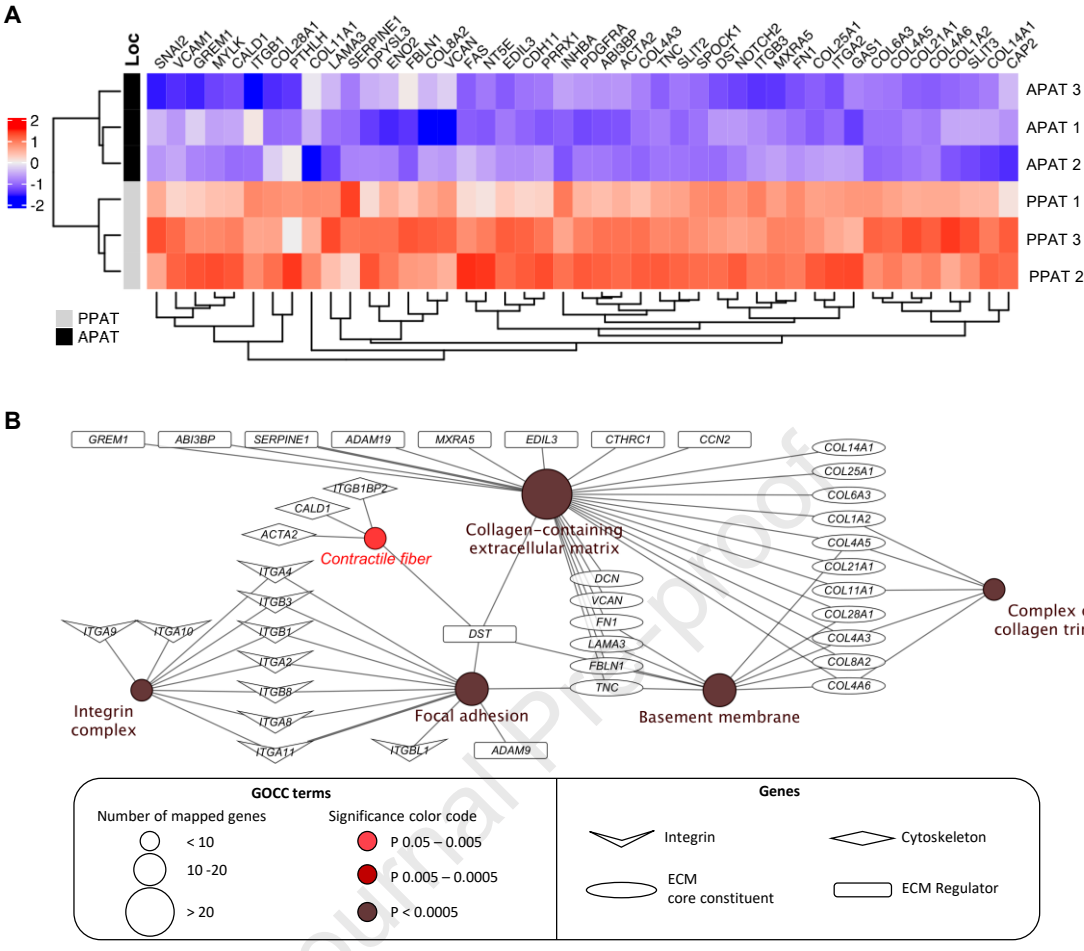

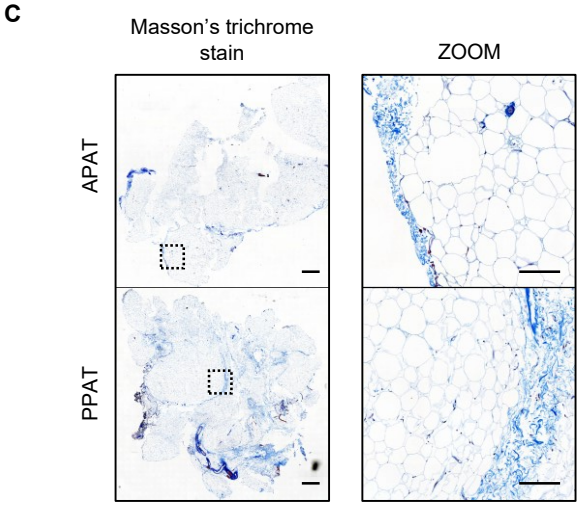

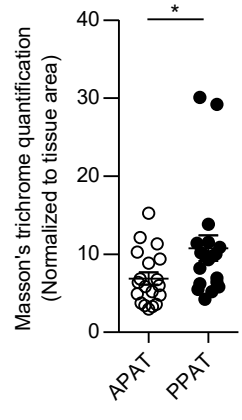

Figure 6

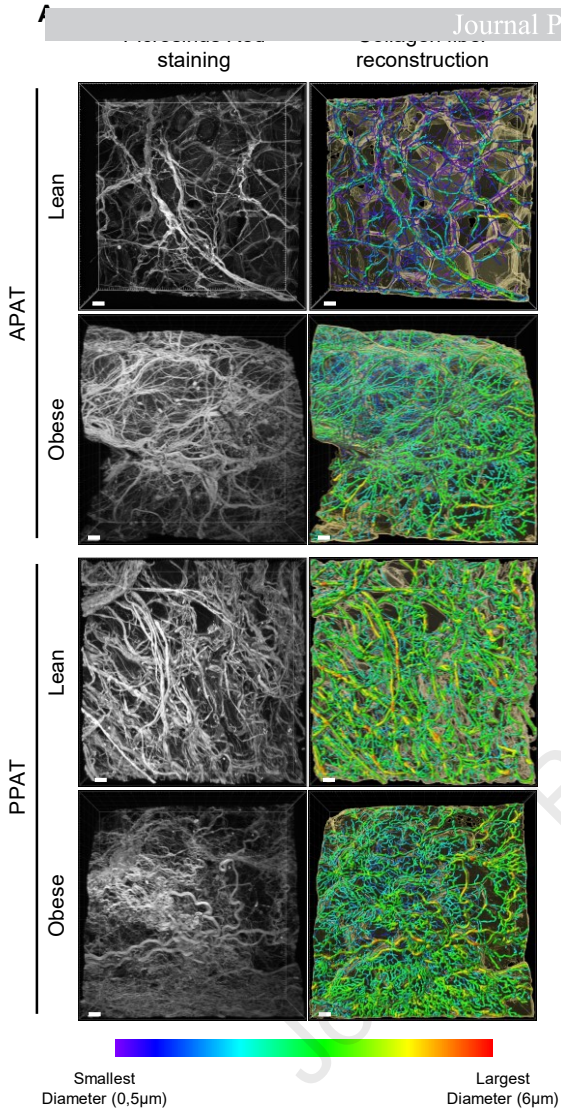

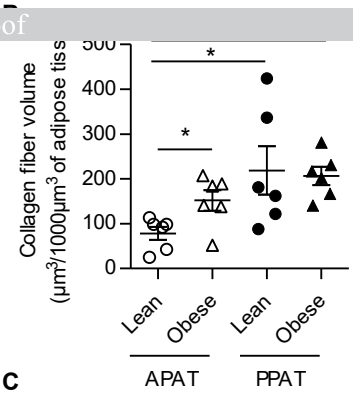

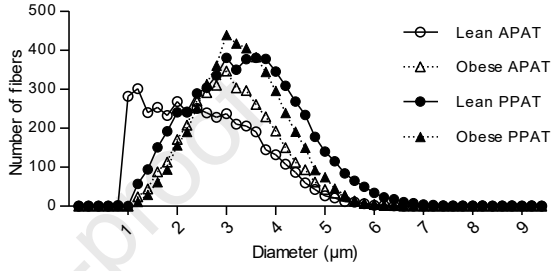

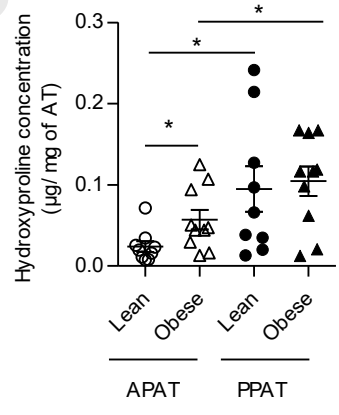

Figure 7